



Ultralow Emittance Thermal Radiation Barrier Achieved by a High-Contrast Grating Coating

Richard Z. Zhang*¹ and Ken Araki[†]
 University of North Texas, Denton, Texas 76207

<https://doi.org/10.2514/1.T6636>

Thermal radiative emission in vacuum is minimized using metal-backed flexible “space blankets” that have a theoretical minimum infrared emittance of 0.03. However, their presence under oxygenated and degradation-prone environments rapidly increases emittance due to metal oxidation, surface pitting, and implantation of contaminants. A monolithic dielectric coating composed of microscale periodic metasurface gratings on multilayers and metal thin film can achieve sub-1% total emittance. The minimum emittance can be tailored to any temperature-function blackbody emission, so long as the selected dielectric coating materials have near-zero absorption. Using computational optimization and theoretical understanding of high-contrast grating phase-shift mode conditions, we identified characteristic at-wavelength germanium gratings and a near-quarter-wave layer above a low-refractive-index infrared-transparent Fabry–Pérot multilayer interference cavity. This dual mechanism can achieve a room-temperature total emittance of 0.0085, paving a new theoretical minimum multilayer insulation effective conductance. As multilayer insulation, this coating offers total effective emittance of 0.0032 per pair of optimally mismatched grating surfaces. This ultrahigh reflection coating design can also be relevant in thermal management of refrigeration and electronic components.

Nomenclature

c_0	=	speed of light, m/s
d	=	layer thickness, μm
E	=	electric field
f	=	grating width-to-period filling ratio or duty cycle
H	=	magnetic field
h	=	grating height, μm
\hbar	=	Planck constant, $\text{J} \cdot \text{s}$
k	=	wave vector, rad/m
k_B	=	Boltzmann constant, J/K
N	=	orders or layers
n	=	refractive index
q	=	eigenvalue
r	=	Fresnel reflection coefficient
S	=	surface roughness scattering coefficient
T	=	temperature, $^\circ\text{C}$ or K
t	=	Fresnel transmission coefficient
v	=	eigenvector
w	=	grating width, μm
α	=	absorptance
β	=	lateral wave vector, rad/m
δ	=	root-mean-square roughness, nm
ϵ	=	emittance
Θ	=	Planck blackbody function, $\text{W}/(\mu\text{m} \cdot \text{m}^2)$
θ	=	incident angle, rad or deg
κ	=	absorption coefficient
Λ	=	grating period, μm
λ	=	wavelength, μm
ρ	=	reflectance
σ	=	Stefan–Boltzmann constant, $\text{W}/(\text{m}^2 \cdot \text{K}^4)$
τ	=	transmittance
ψ	=	phase, rad/s
ω	=	frequency, rad/s

Subscripts

b	=	back
f	=	front
Gr	=	grating
H	=	hemispherical
h	=	high-refractive-index material
inc	=	incident
l	=	low-refractive-index material
m	=	metal layer
n	=	normal incident
p	=	plasma
r	=	roughness
rms	=	root mean square
sub	=	substrate
TE	=	transverse electric
TM	=	transverse magnetic

Superscript

*	=	effective
---	---	-----------

I. Introduction

Thermal radiative coupling between surfaces is minimized with metallic coatings or thin films. These radiation sheet barriers are used in various thermal management applications, such as spacecraft space blankets, refrigeration component insulation, household climate control, and many others. The effective conductance of layered metallized blankets called multilayer insulation is minimized with more layers and a vacuum environment [1]. The mechanism that allows thermal decoupling is due to low photonic emittance (high reflectance) surfaces. Traditionally, these surfaces consist of submicrometer-thin physical vapor deposited metals because their electrical conductance results in field cancellation from external electromagnetic waves [2,3]. Transition metals such as aluminum, copper, gold, silver, and others are free electron dense, resulting in high plasma frequency, as described by the Drude free electron damping model [3,4]. With these metals, the low-energy gap between oxidation states combined with the metal bond lattice ductility makes them susceptible to degradation of optical properties [5,6]. Thickness-dependent formation of surface oxidation and defects can increase infrared emittance by severalfold, whereas typical submicrometer root-mean-square roughening can increase visible to near-infrared wavelength absorptivity from solar

Received 19 April 2022; revision received 28 June 2022; accepted for publication 5 July 2022; published online 24 August 2022. Copyright © 2022 by the American Institute of Aeronautics and Astronautics, Inc. All rights reserved. All requests for copying and permission to reprint should be submitted to CCC at www.copyright.com; employ the eISSN 1533-6808 to initiate your request. See also AIAA Rights and Permissions www.aiaa.org/randp.

*Assistant Professor, Department of Mechanical Engineering; zihao.zhang@unt.edu (Corresponding Author).

[†]Graduate Research Assistant, Department of Mechanical Engineering.

radiation [7–9]. In spaceflight environments, the optical properties of coatings quickly degrade over the first two years due to surface pitting from outgassing, micrometeoroids or debris, high-energy particle radiation, and atomic oxygen in low Earth orbit [1,10,11]. To resist mechanical and optical degradation of these metal films on flexible polymer substrates, manufacturers apply micrometer-thick surface finishes such as silica, indium tin oxide, germanium, and transparent polymers [1,2,12]. As a means to improve these surface finishes, we propose a scalable micropatterned optical coating that both protects against physical degradation and improves the infrared thermal radiative performance.

Several mechanisms can achieve high reflectance without a plain metal mirror. One mechanism is Fabry–Pérot interferometry, which produces near-perfect resonant reflection and transmission by designing appropriate transparent material thicknesses and refractive index contrast [3,13]. Fabry–Pérot cavities typically contain a low-refractive-index transparent insulator cavity layer surrounded by high-refractive-index thin-film boundaries. This traditional Fabry–Pérot mechanism has been linked with multilayer Bragg mirrors [3,14], fiber-optic waveguides [15], laser resonators [16], perfect radiative absorbers [17,18], and Michelson interferometry for vibrational and thermal detection [19,20]. More recently, the Fabry–Pérot mechanism helped achieve potential spacecraft radiator switching on and off of near-unity emittance using insulating-to-metal temperature phase transition materials, such as vanadium dioxide (VO_2) [21–23]. The Fabry–Pérot interference quality is additive; a very large number of periods of cavity quarter-wave multilayers can enable perfect transmission or reflectance. However, in the interest of minimizing the thickness of a monolithic coating, a complementary resonant mechanism should be considered.

The second and somewhat similar mechanism is the high-contrast grating (HCG), which a periodically patterned microstructured meta-surface that acts as a phase-shift mode waveguide [24]. This unique type of grating design is attributed to Constance Chang-Hasnain and co-authors, and since the mid-2000s was originally applied to mirrors in vertical cavity surface emitting lasers (VCSELs) [24–26]. HCG can obtain high-quality broadband reflectance exceeding 0.99 at normal incidence by virtue of high-refractive-index structures having a period or duty cycle comparable to the wavelength surrounded by a low-index medium: typically vacuum [27–29]. Monolithic HCG constructions on optical thin films have also been used in electro-mechanical tunable mirrors, optical resonators and switches, thermal emitters, and more [30,31]. Interestingly, there has yet to be a formal assignment of HCG in ultrahigh reflectance metasurfaces toward a more effective thermal insulation. This paper examines the optical interference mechanisms of HCG on its own and in assistance to the Fabry–Pérot cavity as a performance thermal reflector.

We also recognize the nonradiative means to provide ultralow thermal transport. Aerogel, which is a nanoporous silica, can achieve thermal conductance as low as $8 \text{ mW}/(\text{m} \cdot \text{K})$ [32]. A boron nitride nanotube embedded polymer gel could maintain low thermal conductance in a high-temperature condition, outperforming sole polymer substrates [33]. However, a big weakness with mixed-phase gas effective medium foams, slabs, and paints is their outgassing between

atmospheric and vacuum pressures, creating vacancies and tears in films [1]. Although recent interest in sustainable, renewable, and bioinspired building insulation materials has surfaced to address material impact on the terrestrial environment and climate, their endurance and performance in demanding environments have yet to be assessed [34,35]. In this study, we identify materials and pattern designs that can obtain lower infrared radiative emittance than pristine metal. A survey of existing thin-film coating materials assesses the suitability of their thermal insulative performance. With a set of ideal materials, we study the both Fabry–Pérot and HCG optical mechanisms for achieving near-perfect reflectance. Variations in coating designs at corresponding temperature conditions and integration into multilayers are evaluated for effective conductance performance in vacuum. The goals of this investigation are to obtain a perfect infrared mirror and to elaborate the design values for tailorable radiative insulation conditions. The concept of a protective coating exceeding the reflectance of the existing metal thin-film substrate could impact the engineering of compact and resilient spacecraft architectures, building insulation and fire protection as well as cryogenic device thermal management.

II. Parameters and Computational Methodology

This section describes materials' selection, their optical properties, and calculation of radiative properties of both Fabry–Pérot multilayers and periodic gratings. The combined configuration illustration of the HCG and Fabry–Pérot coating, as well as their representative material types, is represented in Fig. 1. The grating period is Λ , its width is w , and its height is h . Two-dimensional (2-D) high-contrast gratings have dimensions Λ and w in both x and y . The multilayer thicknesses are d . The material or layers' refractive indices are designated by n . The uppermost layer (blue) consists of the high-refractive-index material for HCG and the Fabry–Pérot boundaries. The Fabry–Pérot cavity layer (green) is a low-refractive-index material. This is on top of metal thin film, which is typically no more than a few hundred nanometers thick. A structural substrate can be used to allow flexibility and is made of polymers. The other side can optionally be coated to further reduce radiative coupling.

A. Optical Properties of Materials

In selecting materials comprising the coating, the imaginary component or absorption coefficient of the refractive index should be minimal for the wavelength range of interest. To minimize absorption from solar irradiation or emission from high-temperature blackbodies via Kirchhoff's law of radiation, a dielectric or insulator must have a near-zero imaginary component of the refractive index κ in the visible ($\lambda = 0.4\text{--}0.7 \mu\text{m}$) and up to the near/short infrared ($\lambda = 0.7\text{--}3 \mu\text{m}$). To minimize emission from terrestrial or room-temperature bodies, the transparency region is between $\lambda = 3 \mu\text{m}$ and beyond $30 \mu\text{m}$, which is the mid- to far-infrared range. For cryogenic and subkelvin bodies, the transparency region in the wavelength of interest may be complicated because it could lie in the microwave ($\lambda > 1000 \mu\text{m}$). On the other hand, materials to be used for the metal substrate are less varied and less rigorous. Consideration

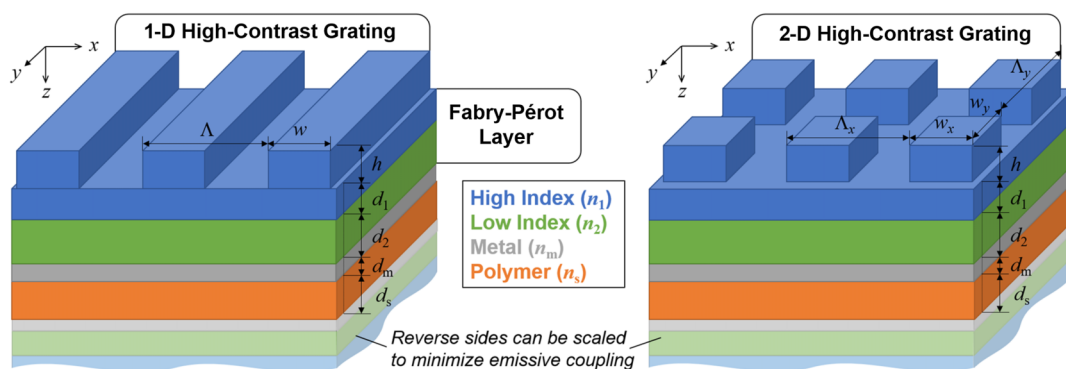


Fig. 1 Illustrated schematic of materials and nomenclature of the combined high-contrast grating and Fabry–Pérot radiative coatings.

for metals is rather on its high plasma frequency ω_p dependency in the short wavelength UV-visible range spectrum, where aluminum (15 eV) exceeds that of gold, silver, and copper (7–9 eV) [3,4,36]. Moreover, appropriate environmental conditions on these metals must also be weighted. The structural polymer material type is mostly dictated by mechanical strength and stability in operating temperatures; the polymer may participate in radiative exchange in single-side coated sheets.

Table 1 outlines some candidate dielectrics, metals, and polymer materials for radiative barriers under high-temperature applications and under room-temperature applications. For each category, the preferred material is listed first. The visible to near-infrared range is considered for minimizing solar absorptivity α . For high-index dielectrics having transparency windows from 300 nm up to 10 μm , hafnium oxide (HfO_2) and tantalum pentoxide (Ta_2O_5) have near-constant refractive indices of $n = 1.9$ and $n = 2.1$, respectively [37,38]. These heavy transition metal oxides present interband electron resonance, resulting in broad Lorentz high- κ absorption peaks centered around the mid- and far infrared [3]. The more ubiquitous silicon dioxide (SiO_2) or quartz crystal is a low-refractive-index material with $n = 1.5$ from the visible wavelengths up to 7.5 μm [39,40]. To reach a lower refractive index, mineral fluorides may provide good alternatives. For example, calcium fluoride (CaF_2) has transparency up to around 19 μm , with a refractive index around $n = 1.4$ [41]. Metal thin film with a high free electron density is preferred, such as aluminum (Al) and possibly copper (Cu), so that frequencies beyond plasma oscillations lie in the extreme UV [3,8,42]. Gold (Au) and Silver (Ag) are other possible metal films. Lastly, the polymer material can vary among Kapton (polyimide), biaxially-oriented polyethylene terephthalate (BoPET or MylarTM), and polytetrafluoroethylene (PTFE or TeflonTM). Orange-colored Kapton is thermally stable, but it presents the highest natural absorptance and emittance due to its multitude of broad and narrow phonon absorption peaks in the infrared [43,44]. Clear Mylar presents better optical properties but degrades under the sun [1,45]. Teflon is similar to Kapton in its infrared emittance and has better transparency under the solar spectrum; Teflon is used as a spacecraft optical solar reflector, but its temperature tolerance window (–200 to +260°C) is narrower than Kapton's (–269 to +400°C) [1,43]. These tradeoffs can be more seriously considered at the manufacturers' discretion.

For targeting room-temperature operation radiative insulation, the high-refractive-index dielectric can be either germanium (Ge) or silicon (Si). Ge has the highest refractive index of $n = 4.0$ through all infrared wavelengths, but it is absorbing at wavelengths below 1 μm [46]. The Ge crystal structure is face-centered cubic and can be amorphous with little change to electron band function, but Ge becomes conductive above 350 K as thermal electrons enter the band gap [47]. Undoped Si has a slightly lower refractive index of $n = 3.4$, from the visible to the far infrared [48]. For the low-index dielectric materials, the candidate pool becomes limited as the bound electron absorption of oxides occurs in the mid- to far-infrared. CaF_2 also becomes too absorbing, where its Reststrahlen peak or Lorentz resonance is centered near 40 μm . Heavy mineral fluorides also with $n \approx 1.5$, such as barium fluoride (BaF_2), have their Reststrahlen peak centered near 50 μm [47]. Another class of infrared-transparent dielectrics includes heavier halogen salts, and bromides. Cubic potassium bromide (KBr) has been used in infrared-transparent glasses because its Reststrahlen peak lies beyond 70 μm and its infrared refractive index is just slightly higher at $n = 1.55$ [49]. In

the case study of low emittance coating design for room-temperature conditions, we choose Ge and KBr for their offering of highest-refractive-index contrast as well as transparency in the broad infrared wavelengths matching the Planck blackbody function at 300 K.

From this material survey, we compare the effect of imperfect or degraded metallized thin film on spectral solar absorptance and infrared emittance. We also model and compare the spectra of pre-existing protective thin-film coating solutions used by metallized blanket manufacturers. The spectral normal absorptance is designated by $\alpha_{n,\lambda}$, and the spectral normal emittance is designated by $\epsilon_{n,\lambda}$. At normal incidence from vacuum and through a layer of thickness d_1 having a complex refractive index n_1 on an opaque large-index metal, the thin-film equation can be approximated by

$$\alpha_{n,\lambda}, \epsilon_{n,\lambda} = 1 - \left| \frac{(1 - n_1) - (1 + n_1)e^{A_{\text{ind}}n_1/\lambda}}{(1 + n_1) - (1 - n_1)e^{A_{\text{ind}}n_1/\lambda}} \right|^2 \quad (1)$$

For a film with zero κ_1 , and therefore no decay term, $\alpha_{n,\lambda}$ and $\epsilon_{n,\lambda}$ are zero. But, with an attenuating thin film with nonzero κ_1 , this equation becomes more complicated. In Figs. 2a and 2b, flat aluminum is covered with a 20-nm-thick aluminum oxide (Al_2O_3) film having a dielectric function by Query, which is typical under exposure to atmospheric conditions [50]. Compared to bare aluminum experimentally obtained by Ordal et al., the infrared emittance uniformly increases by roughly 0.02 but oxidation does not greatly affect absorptance from visible and near-infrared light [51]. Using a normal incidence, surface roughness, scattering reflectance, coefficient factor $S_{r,n}$ for a 20 nm root mean square δ_{rms} , the term inside the absolute brackets in Eq. (1) is modified by

$$S_{r,n} = e^{-8\pi^2\delta_{\text{rms}}^2n_n^2/\lambda^2} \quad (2)$$

Due to its λ^{-2} scaling, the surface roughness effects are more prominent in the short wavelengths. This is observed in the increase in absorptance in visible radiation wavelengths below 0.7 μm . Therefore, the presence of both a metal surface protective and nonoxide coating can critically improve radiative insulative performance. Silver has better reflectance; but, due to its higher susceptibility to atmospheric and thermal tarnish or corrosion, it requires a protective finish [52].

Protective coatings can offer both degradation protection and electrostatic discharge (ESD) buildup mitigation [1,2]. A polymer coating such as polymethyl methacrylate (PMMA or Acrylic) on the metal side only offers the former. PMMAs, like all the polymer structural substrates, have many narrowband long-chain phonon absorption modes, which were observed by Zhang et al. [45] and Tsuda et al. [53]. From a 300-nm-thick PMMA on aluminum, the spectral emittance shows many peaks in the mid- and far infrared, as well as a minimal increase in absorptance in the visible wavelength range. Silicon oxide (SiO), which is slightly more favorable than SiO_2 due to its slightly narrower Lorentz absorption centered around $\lambda_0 = 10 \mu\text{m}$, drastically increases infrared emittance. SiO is only for preventing mechanical burnishing. In consideration of the materials presented in Table 1, we apply a 300-nm-thick layer of KBr with a dielectric function from Palik, and the infrared emittance is minimally affected [49]. This layer of infrared-transparent coating presents similar absorptance and emittance spectra as the PMMA polymer but without the narrow absorptance peaks. Although not shown in Fig. 2d, a 300-nm-thick layer of vacuum-deposited Ge defined by Amotchkina and Porter on aluminum demonstrates high emittance due to its high refractive index, as well as high absorptance due to its phonons [47]. A layer of Ge around 50 nm or thinner can reduce its constructive interference in the infrared. Section III explores the appropriate thicknesses needed to minimize emittance using infrared glasses of KBr and Ge.

B. Rigorous Coupled-Wave Analysis

Rigorous coupled-wave analysis (RCWA) is used to obtain the optical properties and electromagnetic field of the periodic structures. The RCWA formulations are derived from Fourier expanded wave equations [54,55]. The electric E_{Gr} and magnetic H_{Gr} fields in the

Table 1 Coating materials targeting visible to near-/short-infrared, and mid- to far-infrared wavelengths [10]

	Visible to near/short IR (0.3–2.4 μm)	Mid- to far IR (5.0–35 μm)
High index	HfO_2 [37], Ta_2O_5 [38]	Ge [47], Si [3]
Low index	SiO_2 [40], CaF_2 [41]	BaF_2 [41], KBr [49]
Metal [3,4]	Al, Cu	Al, Ag, Au
Substrate	Kapton [44], Mylar [45], Teflon [43]	

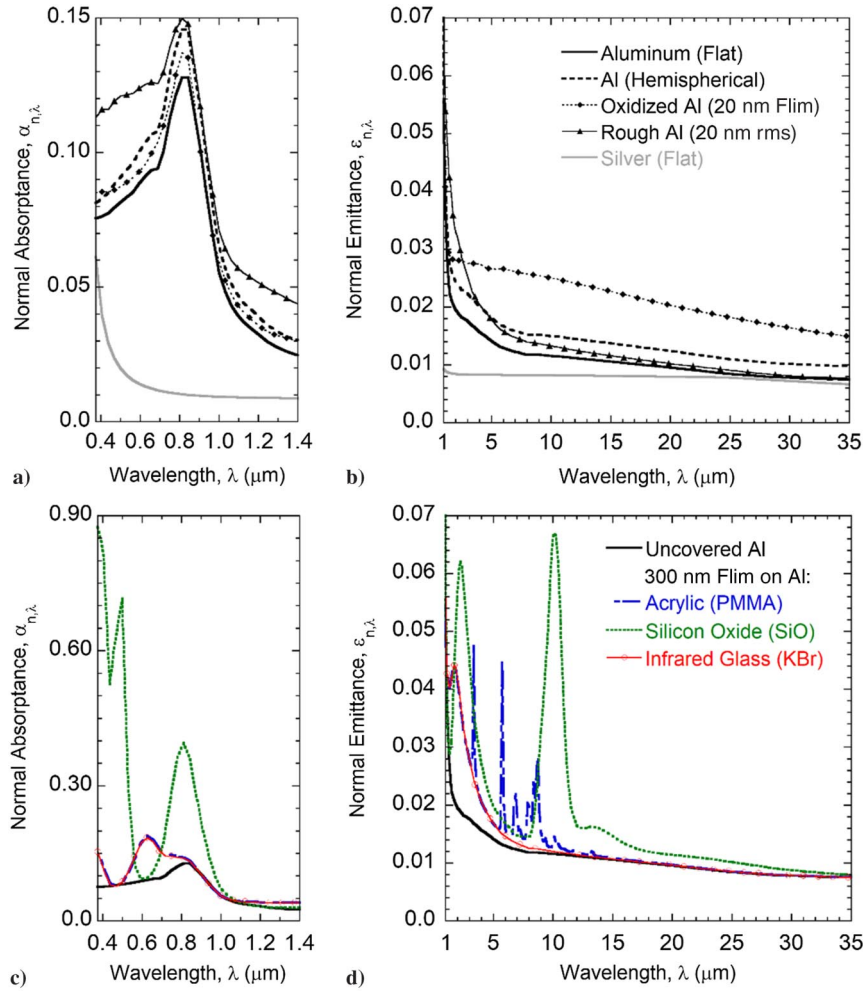


Fig. 2 Absorbance (Fig. 2a) and emittance spectra (Fig. 2b) of aluminum, its after effects, and silver. Absorbance (Fig. 2c) and emittance spectra (Fig. 2d) of protective films.

simple grating shown in the uppermost layer in Fig. 1 are calculated by the Fourier expansion of the space-harmonic field terms:

$$E_{\text{Gr}} = \sum_j E_j(z) \exp(ik_{x,j}x) \quad (3a)$$

$$H_{\text{Gr}} = i \sqrt{\frac{\epsilon_0}{\mu_0}} \sum_j H_j(z) \exp(ik_{x,j}x) \quad (3b)$$

where E_j and H_j are the amplitudes of the space-harmonic component fields of diffraction orders $j = 0, \pm 1, \pm 2, \dots, \pm N$. For all cases of one-dimensional (1-D) RCWA, the order number is $N = 19$, which is more than adequate for far-field radiative properties of nonplasmonic gratings [56]. Note that $k_{x,j}$ is the lateral wave vector, which is decomposed into $k_{x,j} = 2\pi \sin \theta / \lambda + 2\pi j / \Lambda$ [3]. Equations (3a) and (3b) are substituted into the coupled-wave system of equations, which is given by

$$\sum_j \left[\frac{1}{k_0^2} \frac{\partial^2 E_j}{\partial z^2} - \frac{k_{x,j}^2}{k_0^2} E_j + \sum_p n_{j-p}^2(x) E_p \right] = 0 \quad (4)$$

where the refractive index in the grating region is expanded into a Fourier series such that $n_{j-p} = 0$ when $j = p$ [54,55]. This coupled-wave equation can be expressed in a $(2N + 1) \times (2N + 1)$ matrix, which is solved by using the boundary conditions at the surface ($z = 0$) for the electric field and the tangential component of the magnetic field at the interface between the incident and the grating region, as well as the grating and the substrate. E_j can be expressed

with a large number of reflected mode eigenvalues q_m and eigenvectors v_m with forward- and backward-propagating wave coefficients $A_{j,m}$ and $B_{j,m}$, respectively. The grating diffraction-order-dependent reflection r_j and transmission coefficients t_j can then be solved in matrix operations using

$$r_j + r_0 = \sum_{m=0}^{\infty} v_{j,m} [A_{j,m} + B_{j,m} \exp(-k_0 q_m d)] \quad (5a)$$

$$t_j = \sum_{m=0}^{\infty} v_{j,m} [A_{j,m} \exp(-k_0 q_m d) - B_{j,m}] \quad (5b)$$

where $r_0 = 1$ for $j = 0$, and $r_0 = 0$ for $j \neq 0$. The overall reflectance and transmittance can be obtained from calculating reflected and transmitted diffraction efficiencies defined as

$$DE_{r,j} = r_j r_j^* \text{Re} \left(\frac{k_{\text{inc},j}}{k_0 \cos \theta} \right) \quad (6a)$$

$$DE_{t,j} = t_j t_j^* \text{Re} \left(\frac{k_{\text{sub},j}}{k_0 \cos \theta} \right) \quad (6b)$$

This system of equations obtains the reflectance

$$\rho_\lambda = \sum DE_{r,j}$$

and transmittance

$$\tau_\lambda = \sum DE_{t,j}$$

by applying the same procedure to coupled H_j waves [3,54,55]. The spectral emittance is related via $\varepsilon_\lambda = 1 - \rho_\lambda - \tau_\lambda$.

For a 2-D grating with patterning in both the x and y directions, the azimuthal angles ϕ for both the transverse electric (TE) and transverse magnetic (TM) waves are also included. With diffraction orders of j for the x direction and l for the y direction, the grating electromagnetic fields are calculated using [57–59]

$$E_{\text{Gr}} = \sum_{j,l} [E_{x,jl}(z)\hat{i} + E_{y,jl}(z)\hat{j} + E_{z,jl}(z)\hat{k}] \exp[i(k_{x,j}x + k_{y,l}y + k_{z,jl}z)] \quad (7a)$$

$$H_{\text{Gr}} = i\sqrt{\frac{\varepsilon_0}{\mu_0}} \sum_{j,l} [H_{x,jl}(z)\hat{i} + H_{y,jl}(z)\hat{j} + H_{z,jl}(z)\hat{k}] \exp[i(k_{x,j}x + k_{y,l}y + k_{z,jl}z)] \quad (7b)$$

where the wave vector for the Bloch–Floquet condition-satisfying diffracted wave can be modified to

$$k_{x,j} = 2\pi n_0 \sin \theta \cos \phi / \lambda + 2\pi j / \Lambda_x$$

and

$$k_{y,l} = 2\pi n_0 \sin \theta \sin \phi / \lambda + 2\pi l / \Lambda_y$$

where $l = 0, \pm 1, \pm 2, \dots, \pm M$ [59]. The 2-D RCWA becomes a much more time-consuming calculation due to differing $(2N + 1)$ th versus $(2M + 1)$ th terms representing x and y diffraction order matrix calculations, respectively [59].

The total normal emittance as a function of the spectral normal emittance is given by

$$\varepsilon_n = \frac{\int_0^\infty \varepsilon_{n,\lambda} \Theta(\lambda, T) d\lambda}{\sigma T^4} \quad (8)$$

where the Planck blackbody emissive power wavelength–temperature function is

$$\Theta(\lambda, T) = 2\hbar c_0^2 / \lambda^5 (e^{\hbar c_0 / \lambda k_B T} - 1)$$

when provided the universal thermophysical constants c_0 , k_B , and σ . Note that the integration from a finite nonzero lower bound wavelength and a noninfinity upper bound wavelength requires numerical integration of the denominator of Eq. (8) as $\varepsilon_{n,\lambda} = 1$. The typical separation distance between insulation sheets is no less than 160 μm , which is provided by low-conductivity fabric mesh netting [1]. Because this far-field radiative gap distance can be regarded as a unity radiative view factor between two infinite parallel surfaces, normal emittance between surfaces is prioritized [60].

III. Theory and Principles of High Reflectance

To target room-temperature ($T = 300$ K) blackbody emission, the following discussions select far-infrared-transparent glasses to understand and illustrate optical mechanisms of Fabry–Pérot interference and moded HCG reflectance. Germanium is chosen as the high-refractive-index crystal, and potassium bromide is chosen as the low-refractive-index crystal. Pure and undoped Ge is transparent in the far infrared and up to radio frequencies, but it is not transparent in the visible range.

A. Fabry–Pérot Layer

The simplest first-order structure to maximize reflectance is the Fabry–Pérot (FP) multilayer. The thicknesses that describe the FP are determined by the quarter-wave equation as a function of the layer's real

part of the refractive index: $d = \lambda_0 / 4n$, where λ_0 is the center wavelength of maximum reflectance. Typically, this wavelength corresponds to the Wien displacement law with the blackbody temperature, which is given by $\lambda_0 (\mu\text{m}) = 2898 / T(\text{K})$. The thickness of the FP cavity is determined by the half-mode phase shifts ψ at normal incidence, where $\psi = 2\pi \text{Re}(n_i) / \lambda_0 = 0.5\pi, 1.5\pi, 2.5\pi, \dots$ [3,56].

When integrating spectral normal emittance across the Planck spectrum for a $T = 300$ K blackbody to obtain minimum total absorptance, we found that the center wavelength is higher than that determined by the Wien displacement law. This is because the Planck emissive power at longer wavelengths is more prominent than the wavelengths below the function's peak. Here, we apply that $\lambda_0 = 11.7 \mu\text{m}$. In Fig. 3, the high-quality reflectance maximization can be shown for one pair of FP quarter-wave layers: $d_1 = 0.74 \mu\text{m}$ Ge above $d_2 = 1.593 \mu\text{m}$ KBr. For this configuration, the lowest emittance of $\varepsilon_{n,\lambda} = 1.64 \times 10^{-3}$ occurs at $\lambda = 12.1 \mu\text{m}$. The calculated total normal emittance for a blackbody at 300 K is then $\varepsilon = 0.011$, matching that of pure flat aluminum. When applied with an identical second pair of FP layers above the first pair, we expect the emittance to further decrease. Although this is true at the center wavelength, where the minimum is $\varepsilon_{n,\lambda} = 2.5 \times 10^{-4}$ at $\lambda = 11.7 \mu\text{m}$, the surrounding spectrum has broad high emittance interference peaks. With this secondary layer, the total normal emittance at room temperature increases to $\varepsilon = 0.012$. With more and more layers, the wavelength region around λ_0 becomes a Bragg reflector stop band between $\lambda / (d_1 + d_2) = 3.5$ and 6.25 [3]. In the wavelength regions outside this stop band, the passband, the oscillations become more frequent and higher magnitude with increasing layers due to thin-film interference. One should also

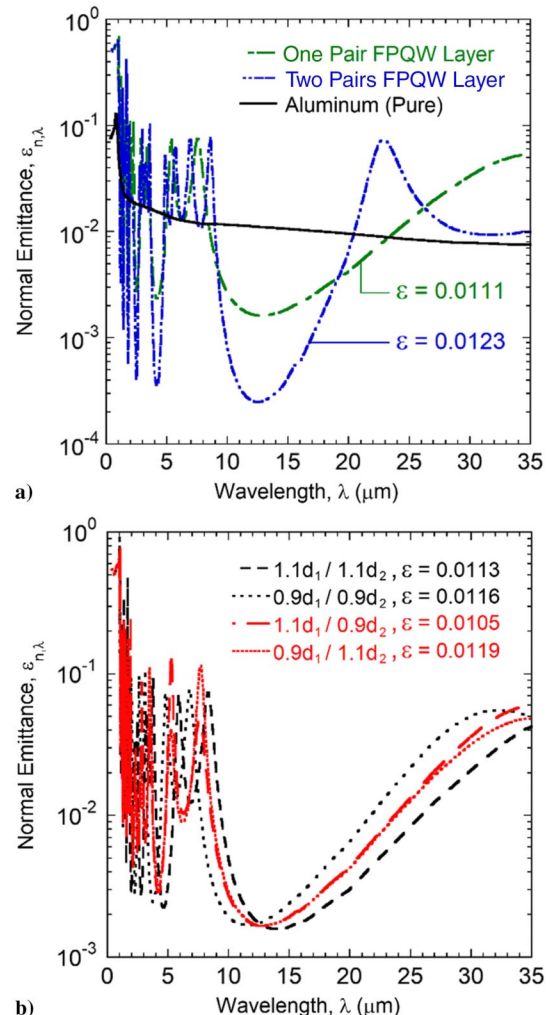


Fig. 3 Spectral and total emittance of a) Ge/KBr Fabry–Pérot quarter-wave (FPQW) pairs, and b) sensitivity from $\pm 10\%$ variation of single-pair FPQW thicknesses.

not lose sight of the thickness of the coating because each FP pair is $2.33 \mu\text{m}$ thick in this material configuration.

With one pair of FP layers sufficient to achieve emittance below that of the metallic substrate, we test the consequence of slight imperfections in FP layer thicknesses. Figure 3b plots the spectra for each layer 10% thicker and thinner than the designed quarter-wave thickness. Each layer being 10% thicker has little effect on the total normal emittance because the emittance minimum is slightly decreased and redshifted. The redshifting of the multiple narrow interference fringes at wavelengths below this stop band contribute to the slight increase in total emittance. This effect is similar with 10% thinner layers but in the opposite direction. The emittance peak in the far infrared beyond $35 \mu\text{m}$ is now visible in the spectrum, for which its integration weighted with the Planck blackbody function increases the total emittance further. The last two variations are interestingly mixed. A thicker high-index (Ge) layer and thinner low-index (KBr) layer results in even lower total emittance. The stop band is unchanged from the perfect quarter-wave case, but the interference fringe magnitude just below this ($\lambda = 7.1 \mu\text{m}$) is decreased. The emittance in the stop band is also preserved for the thinner Ge layer and thicker KBr layer, but a more prominent peak appears at the first interference fringe below the stop band. The last two configurations have interference fringe peaks exchange magnitudes in the passband wavelengths between approximately 5 and $10 \mu\text{m}$. Although it can be said that the total thickness of the combination of the FP near-quarter-wave layers may be the determining factor of the emittance minima and maxima, the correlation is not quite linear. Generally, the greater contributing factor to phase shift is the lesser thickness of the interference cavity because $\psi \propto d_2$.

B. High-Contrast Grating

This section studies how standalone high-contrast gratings can achieve broadband near-perfect reflection without a metallic substrate. The HCG material is selected as germanium due to its highest nonmetallic and zero-attenuation refractive index ($n \sim 4 + 0i$) contrasting with the air/vacuum or a low-refractive-index substrate in the broad infrared spectrum. The basic radiative properties of 1-D HCG are calculated with Eqs. (3–6), whereas radiative properties of 2-D HCG are calculated with Eq. (7). This section seeks to optimize the HCG dimensions: grating period Λ , grating height h , and grating filling ratio $f = w/\Lambda$.

The contour plots obtaining parameterizations of both the non-dimensionalized grating height and grating period with respect to the wavelength spectrum are shown in Fig. 4. The reflectance contours are averaged over both TE-wave and TM polarizations. Filling ratios are selected as $f = 0.5$, $f = 0.7$, and $f = 0.9$ for the standalone Ge HCG in Figs. 4a–4c, respectively. The blue lines outline the characteristic at-wavelength dual-mode band high reflectance region, and the green lines show the first three TM_0 and TE_2 Fabry–Pérot waveguide modes of the HCG resonance condition dispersion. The local reflectance maxima exceeding $\rho > 0.999$ ($\epsilon < 10^{-3}$) are marked in magenta. The broadest reflectance maxima occur within the HCG-characteristic dual-mode band, which is outlined by the wavelength region bounded by blue lines. At nondimensional wavelengths below the dual-band region ($\lambda < \Lambda$), the high number of interference fringes correspond to diffractive optics [61,62]. To the right of this region ($\lambda \gg \Lambda$), the gratings are subwavelength, and thus becomes effective media. Although it is naturally inclined to increase the filling ratio close to unity due to the increasing broadness of the dual-mode band, the magnitude of reflectance decreases within the dual-mode band. The increased filling ratio shows fewer marked maxima and where the HCG thickness tends toward the waveguide mode ($h > \Lambda$). This tradeoff between the dual-mode band broadness and the magnitude of maximum reflectance lets us establish that the best filling ratio is near $f = 0.7$.

The high reflectance HCG resonance conditions occur using the following dispersion relation for TM-wave polarization [27,28]:

$$k_{\text{Gr},j} \tan\left(\frac{k_{\text{Gr},j} f \Lambda}{2}\right) + n_{\text{Gr}}^2 k_{\text{a},j} \tan\left[\frac{k_{\text{a},j}(1-f)\Lambda}{2}\right] = 0 \quad (9)$$

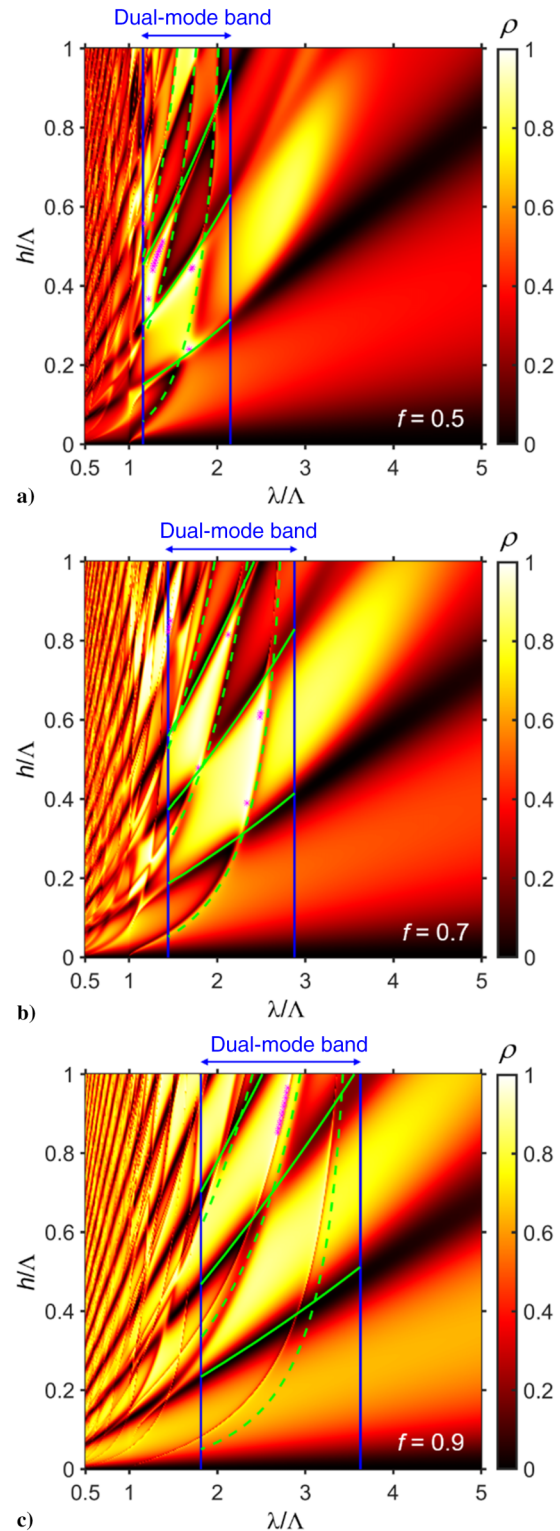


Fig. 4 Normal incidence TE- and TM-averaged period-normalized reflectance spectra of germanium HCG with filling ratios of a) $f = 0.5$, b) $f = 0.7$, and c) $f = 0.9$.

where the j th waveguide mode grating wave vector is given by $k_{\text{Gr},j}^2 = n_{\text{Gr}}^2 k_0^2 - \beta_j^2$, and the air gap wave vector is given by $k_{\text{a},j}^2 = k_0^2 - \beta_j^2$. For the TE polarization, Eq. (9) is modified by only setting $n_{\text{Gr}} = 1$. The dual-mode band cutoff wavelengths λ_2 and λ_4 enclosing the high reflectance regions are obtained by setting $\beta_2 = \beta_4 = 0$ and solving for Eq. (9). For example, for the $f = 0.7$ case, $\lambda_2/\Lambda = 2.88$ and $\lambda_4/\Lambda = 1.44$. This consideration of the dual-mode bandwidth can help determine the HCG period needed to minimize blackbody emission. A 300 K blackbody, for example, would benefit

from an HCG array of a period near $\Lambda = 4 \mu\text{m}$, which is obtained by the Wien displacement maximum to an approximate center wavelength between λ_2 and λ_4 , i.e., $\Lambda = 2898/\lambda T$, where $\lambda \approx 2.5 \mu\text{m}$. This verifies that the characteristic HCG dimension Λ needs to be defined at an infrared wavelength.

The Fabry–Pérot round-trip phase-shift resonance dispersion lines in green, shown in Fig. 4, are for the first three phases ($\psi = 0, \pi$, and 2π). The solid green lines are the first three zeroth waveguide mode TM_0 dispersions, and the dashed green lines are for the second waveguide mode TE_2 dispersions. TM_0 is the dispersion following the $\beta_0 = n_{\text{Gr}}k_0$ light line, and TE_2 for the $\beta_2 - \lambda_2$ second waveguide mode. The first three waveguide modes are outlined because they have the broadest regions of near-unity normal reflectance. In the smallest filling ratio case ($f = 0.5$ in Fig. 4a), the three waveguide modes collapse toward low h/Λ , whereas the third TE_2 mode lies outside the dual-mode band. This low filling ratio does not allow as much high reflectance across broad wavelengths. On the other hand, the high filling ratio ($f = 0.9$) shows dispersions drift toward high h/Λ . Although this seems more promising toward broadband reflectance, the reflectance quality is reduced because the TM modes produce transmission, which is demonstrated by the broader near-zero reflectance near the TM_0 lines. The magenta points enclosed within the upper waveguide modes are the only ρ greater than 0.999. Therefore, the higher filling ratio HCG requires taller gratings, which are attributed to deep groove waveguides [63]. In the intermediate case ($f = 0.7$), the broad reflectance enclosed in the waveguide modes demonstrates high-quality reflectance ($\rho > 0.999$) throughout. Here, we can pinpoint the optimal HCG height, which is close to $h/\Lambda = 0.5$.

To better understand why near-perfect reflectance occurs in the HCG of an optimally selected period, filling ratio, and height, electromagnetic field density plots produced by RCWA are shown in Fig. 5 to visualize and verify planes of constructive and destructive interference. Figure 5 shows an HCG configuration where $\Lambda = 4.4 \mu\text{m}$, $f = 0.7$, and $h = 2.2 \mu\text{m}$. The period was chosen in relation to the Wien displacement center wavelength of $\lambda_0 = 10 \mu\text{m}$, where $\lambda_0/\Lambda = 2.25$. Figure 5a shows the electric field density under the TE-polarized $10 \mu\text{m}$ wave, as well as the in- xz plane magnetic field vectors (H_x and H_z) with white arrows. The three faint field localizations within the Ge HCG structures show that TE waves interact in two Fabry–Pérot round trips [64]. Most importantly, the blue dashed line at exactly $z = 2h$ above the bottom of the grating array shows the HCG-characteristic near-perfect constructive interference of electric fields. Below the grating array, the electric field density is uniformly near zero. Figure 5b confirms this plane of perfect constructive interference as the $|E_x|$ vectors are maximized. We note that the dual round trip occurs in the grating vacuum cavity half-plane because E_x is reversed. We see here that magnetic field localization occurs inside the HCG, which helps produce the electric field phase reversal. In either polarization, the electric and magnetic fields are drastically reduced in the outgoing medium: all without the

use of a metal absorber. Unlike metals, where power densities can accumulate near the surface due to plasmon carrier resonance, the complementary field characteristics and phase reversal inside the lossless HCG can enable fundamental near-zero thermal radiative absorbance.

Additional considerations for HCG design can include expansion into a 2-D array, meaning $\Lambda_x, \Lambda_y, f_x$, and f_y can be distinct. Note that 2-D HCG arrays have additional reflectance bands based on cross-polarization modes, where instead of just TM_0 and TE_2 primary waveguide modes within the dual-mode band wavelengths λ_2 and λ_4 , the primary waveguide modes are $\text{EH}_{00}, \text{EH}_{02}, \text{EH}_{20}$, and EH_{22} within both dual-mode and trimode bands, respectively [64]. The tri mode band represents the 90 deg tilt reflectance between the HCG and creates semibroadband high reflectance resonance conditions approaching the diffraction region ($\lambda \sim \Lambda$). The diffraction region can be interpreted as comprising multimode bands, which produce narrow high and low reflectance conditions, as seen in Fig. 4. Overall, a 2-D HCG purposed for minimizing far-field normal angle incidence and emission radiative exchange does not outperform a well-designed 1-D HCG array. We show the comparison with the best-structured 2-D HCG combined with Fabry–Pérot multilayers in the next section.

IV. Results and Discussion

The combined high reflectance mechanisms of the Fabry–Pérot multilayer and high-contrast grating coating on opaque silver substrate are presented in this section. The FP multilayer comprises one pair of potassium bromide and germanium quarter-wave layers on an opaque aluminum substrate. The HCG array is made of Ge, and the reflectance reduction is compared between 1-D and 2-D HCG cases. All configurations of the combined FP–HCG are realistically on flexible polymer Kapton or Mylar. A double-sided option is also presented, where the opposing-side FP–HCG design can be dimensionally scaled to reflect the blackbody emission of the successive surface. The combined design is then evaluated for its effective thermal emittance reduction performance in a vacuum environment and its role as a multilayer blanket.

A. Monolithic Coating Design

The spectral emittances of multilayers and metasurfaces were calculated using RCWA, which is described by Eqs. (3–6) and Eq. (7) for 1-D structures and 2-D structures, respectively. The 1-D structures are described by the grating parameters period Λ , the filling ratio f , and the height h in the x dimension shown in Fig. 1, whereas 2-D gratings can have distinct periods Λ_x and Λ_y as well as filling ratios f_x and f_y . Figure 6a shows the first iteration of the FP–HCG coating using single-pair FP parameters from Fig. 3a as well as HCG parameters from Fig. 5. The center wavelength for the FP quarter-wave thicknesses corresponds to the Wien displacement

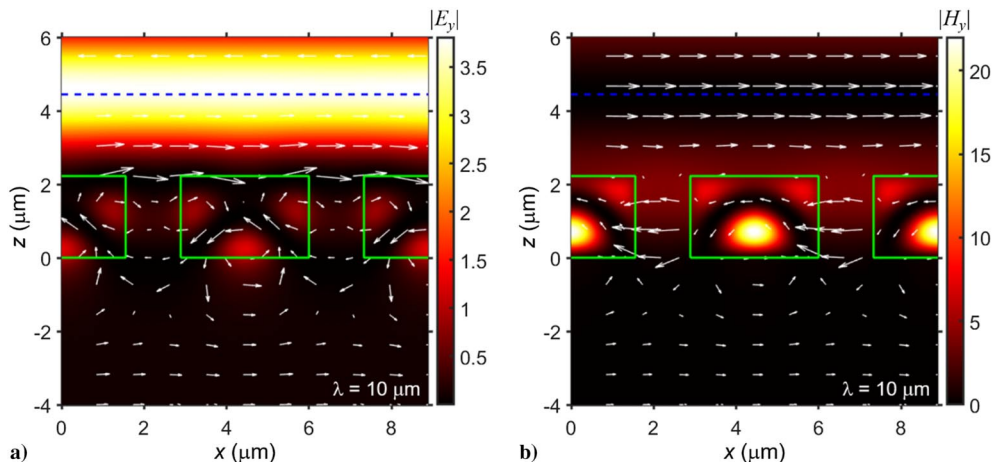


Fig. 5 Electromagnetic field density plots of standalone $\Lambda = 4.4 \mu\text{m}$ germanium HCG in a) TE-wave and b) TM-wave polarizations at $\lambda = 10 \mu\text{m}$.

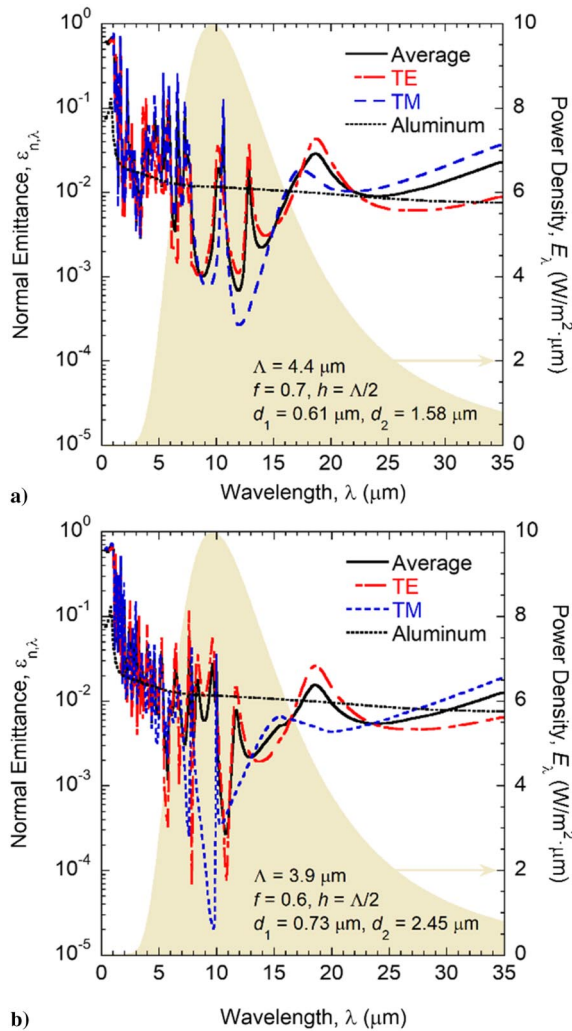


Fig. 6 Normal emittance spectra of Ge-KBr FP and Ge HCG on Al for a) the initial FP-HCG iteration ($\epsilon_n = 0.0138$), and b) the optimized configuration ($\epsilon_n = 0.0085$).

law temperature at 300 K such that $\lambda_0 = 9.66 \mu\text{m}$. The power density function for a 300 K blackbody is plotted in the background of the emittance spectra. The normal emittance spectrum in TE and TM polarizations, and their average, of this FP-HCG combination is given by the parameters: $\Lambda = 4.4 \mu\text{m}$, $f = 0.7$, $h = 2.2 \mu\text{m}$, $d_1 = 0.61 \mu\text{m}$, and $d_2 = 1.58 \mu\text{m}$. The result of the total normal emittance with respect to the 300 K blackbody is $\epsilon_n = 0.0138$, which is averaged over the TE and TM polarizations. As a comparison, the pristine Al spectrum is shown in Fig. 6a, which results in a total normal emittance of $\epsilon_n = 0.0107$. Although this FP-HCG configuration does not outperform the total normal emittance of pristine Al, it can outperform oxidized Al, for which $\epsilon_n = 0.0229$. For the interest of providing sun-facing thermal regulation, the total normal absorptance to a 5778 K blackbody gives $\alpha_n = 0.495$, which is not desired for continuous insolation. Comparatively, the total normal absorptance of both pristine and oxidized Al is near $\alpha_n = 0.08$. The combined FP-HCG design of the initial iteration is not able to lower its total normal emittance from that of the pristine Al substrate.

A parameter fluctuation survey of the FP layer thicknesses is conducted to observe the new normal total emittance minima. In the Supplemental Materials, Fig. S1 shows the layer thicknesses are expanded from $d_1 = 0.61$ to $0.92 \mu\text{m}$ and from $d_2 = 1.58$ to $2.37 \mu\text{m}$. In this paper, the total emittance can be below $\epsilon_n = 0.0138$ for several possible configurations. The layers' thicknesses at $d_1 = 0.84 \mu\text{m}$ and $d_2 = 1.78 \mu\text{m}$ help slightly reduce the total normal emittance to $\epsilon_n = 0.0134$. Also note that the effect on the total normal solar absorptance is nearly negligible with

changes to d_1 and d_2 . Overall, the FP layer thickness variations do not enable total normal emittance below that of pristine Al. A survey of the grating parameters is carried out as well, which is shown in Fig. S2. Changes to the total normal solar absorptance remain small, but the reduction in the total normal emittance is more promising for certain grating parameters. Here, Fig. S2(a) shows broad minimization around grating period $\Lambda = 2.84 \mu\text{m}$ while keeping d_1 , d_2 , f , and h/Λ to their first iteration default. This grating period is much smaller than the predicted period. More importantly, this optimized period resulted in a lower total normal emittance of $\epsilon_n = 0.0101$, which is below that of pristine Al. Selecting the appropriate grating period has a higher impact on minimizing emittance than the filling ratio and the height-period ratio, as shown in Figs. S2b and S2c. Generally, the filling ratio in the selected range near $f \sim 0.6$ and the height-period ratio near $h/\Lambda \sim 0.5$ can certainly minimize emittance, provided the other four covarying parameters are chosen wisely. This kind of simultaneous consideration led to an extensive 50,000 sample corandomized survey of all FP and HCG parameters. Figures S3a through S3e show the absolute total normal emittance with all five parameters: d_1 , d_2 , Λ , f , and h/Λ , respectively. A distinct minimum was found, with clear relationships from Λ and h/Λ but less so from f , d_2 , and d_1 , in that order.

Using the large-sample corandomized survey of FP and HCG parameters, we find that $\Lambda = 3.9 \mu\text{m}$, $f = 0.6$, $h = 1.95 \mu\text{m}$, $d_1 = 0.73 \mu\text{m}$, and $d_2 = 2.45 \mu\text{m}$ result in a total normal emittance of $\epsilon_n = 8.52 \times 10^{-3}$. Additionally, the TE- and TM-polarized total normal emittances are $\epsilon_{\text{TE}} = 0.0106$ and $\epsilon_{\text{TM}} = 6.40 \times 10^{-3}$. Supplemental Fig. S4 demonstrates that ± 10 nm fluctuations on each parameter result in generally less than a 10% total normal emittance increase, with the low-index layer thickness d_2 being the most sensitive. Figure 6b shows the normal emittance spectra of this globally optimized configuration, where the very low TM-polarized normal emittance is evident by the minimum $\epsilon_{n,\lambda} = 2.04 \times 10^{-5}$ at $\lambda = 9.75 \mu\text{m}$, close to the Wien displacement maximum wavelength. Although TE-polarized normal emittance is high ($\epsilon_{n,\lambda} = 0.0428$) at this wavelength, some neighboring wavelengths ($\lambda = 7.88 \mu\text{m}$ and $\lambda = 10.9 \mu\text{m}$) also show emittance minima on the order of $\epsilon_{n,\lambda} = 7 \times 10^{-5}$. Compared to the initial configuration, this optimized configuration achieves lower total emittance due to sharp minima alternating between TE and TM polarizations, whereas the initial configuration maintains less sharp emittance valleys or interference fringes between TE and TM polarizations in phase. In full comparison, the total solar absorptance remains essentially unchanged at $\alpha_n = 0.492$. A dielectric coating's thermal emission reduced below that of the opaque metal substrate is possible; and with a more conductive metal substrate, such as Ag, could result in even lower thermal emission.

For 2-D gratings calculated by RCWA, the calculations are first verified in Supplemental Fig. S5 using the FP-HCG configuration shown in Fig. 6b. The order number of our 2-D RCWA calculations remains at $N = 19$ for each coordinate, giving a total of 361 calculation orders and resulting in a computation time of each case over ~ 1000 s on 12 parallel Intel Xeon E5-2680 2.4 GHz CPUs. There are some slight differences in the spectral emittance minima. For instance, TM-polarized normal emittance is minimum at $\lambda = 9.0 \mu\text{m}$, where $\epsilon_{n,\lambda} = 4.39 \times 10^{-5}$. The total normal emittance of the optimized configuration using our 2-D RCWA resulted in $\epsilon_n = 8.01 \times 10^{-3}$, which is not drastically different. In finding the best 2-D grating configuration, the FP layer thicknesses, grating height, and grating filling ratios in both dimensions are fixed. In Qiao et al.'s study of rectangular high reflectance 2-D HCG on substrate, the filling ratios are the same at $f_x = f_y = 0.6$; whereas the y-direction period is scaled by half of that of x, such that $\Lambda_y = 0.5\Lambda_x$ [27].

Figure 7a confirms this suggested best-case x-y period ratio, where the total normal emittance is minimized at $\Lambda_y = 0.55\Lambda_x$ for $\Lambda_x = 3.9 \mu\text{m}$, $f_x = f_y = 0.6$, and $h = 1.95 \mu\text{m}$. All other grating and multilayer parameters are the same as in Fig. 6b: strictly that $\Lambda_x = 3.9 \mu\text{m}$. The minimum emittance is led by the TM polarization, where $\epsilon_{\text{TM}} = 7.61 \times 10^{-3}$. With the TE polarization ($\epsilon_{\text{TE}} = 0.0128$),

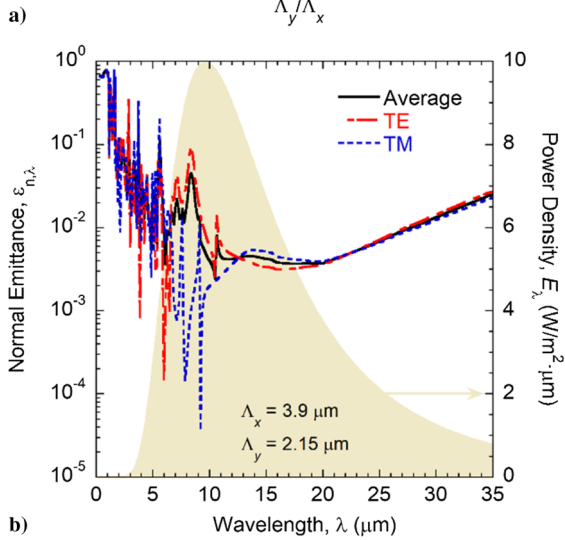
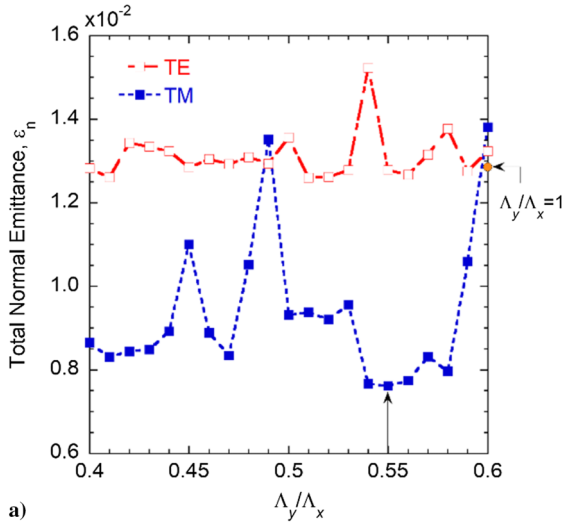


Fig. 7 Relationship of a) total normal emittance in TE and TM polarizations with 2-D HCG period ratio (Λ_y/Λ_x), and b) normal emittance spectra of an optimized 2-D HCG.

the average total normal emittance becomes $\epsilon_n = 0.0102$. Figure 7b shows the normal emittance spectrum for this configuration, where TE- and TM-polarized emittance minima are relatively narrowband as compared to the best 1-D grating case. The only advantage of the 2-D grating is its tempered TE-polarized reflectance fringes in wavelengths beyond the center wavelength: $\lambda_0 > 10 \mu\text{m}$. Although this 2-D grating configuration outperforms pristine Al, it does not outperform the 1-D grating described in Fig. 6b. For square gratings, such that $\Lambda_y = \Lambda_x$, the total normal emittance becomes $\epsilon_n = 0.0128$. For the best design of ultrahigh normal reflectance HCG, long-groove gratings offer the best performance, especially if room-temperature thermal emission and absorption can be just TM-wave polarized. In the consideration of diffuse emission of external surfaces and interlayer thermal exchange, the next section discusses the hemispherical properties and an optimization of a backside-coated thermal insulation flexible blanket.

B. Thermal Insulation Performance

The focus of the previous section assumes that thermal radiative exchange is relevant to only the normal incidence. This assumption holds for multilayer insulation sheets separated by submillimeter distances because radiative transfer is between semi-infinite parallel surfaces. For the interest of off-normal thermal emission, the spectral emittance of the optimized FP-HCG configuration provided by Fig. 6b is hemispherically integrated [3,65]. Figure 8a shows the hemispherical emittance spectra, where the integrated total hemispherical emittance of the coating on Al substrate is $\epsilon_H = 0.0144$.

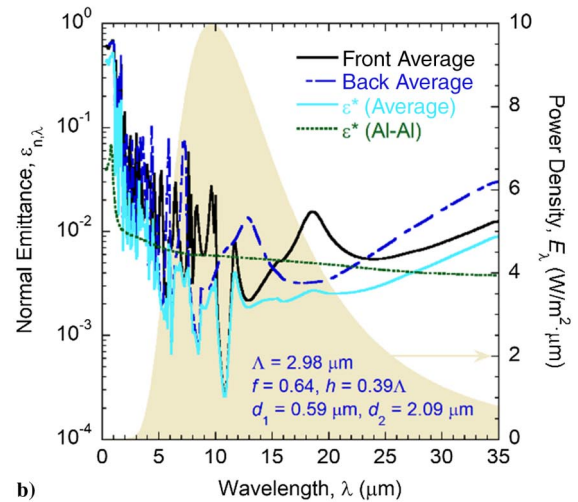
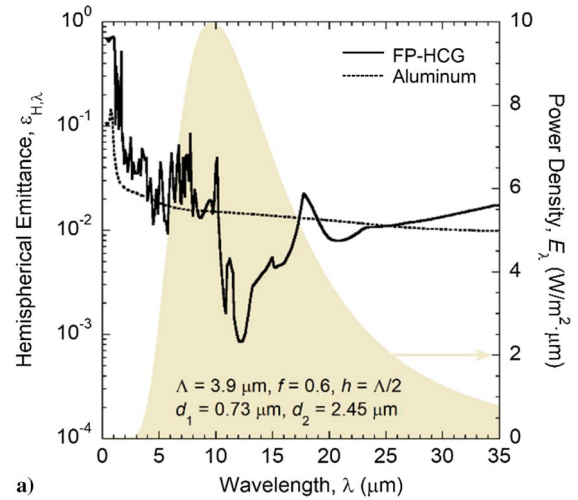


Fig. 8 Spectra of a) hemispherical emittance of the optimized coating from Fig. 6b, and b) normal and effective emittance of mismatched double-sided FP-HCG.

The total hemispherical absorptance is $\alpha_H = 0.551$, which is higher than its normal emittance. The comparison to pristine Al gives a total hemispherical emittance of $\epsilon_H = 0.0133$. The relatively low total hemispherical emittance of the FP-HCG-coated Al is due to the broadband emittance minimization near $\lambda = 12.25 \mu\text{m}$, where $\epsilon_{H,\lambda} = 8.47 \times 10^{-4}$. This configuration's wavelength and angular incidence dependence of the TE- and TM-wave emittances are shown in Supplemental Fig. S6. It explains the low overall emittance in the 10 to 15 μm wavelength region due to TM-wave HCG resonance dispersion. The overall low hemispherical emittance of the coating suggests good performance for low thermal exchange external surfaces or obliquely oriented objects.

In the evaluation of radiative exchange between semi-infinite parallel coated blankets, we assess the effective emittance or “e-star” (ϵ^*) at normal incidence, which is described by [1]

$$\epsilon^* = \frac{1}{\sum_{n=1}^{N-1} \left(\frac{1}{\epsilon_{f,n}} + \frac{1}{\epsilon_{b,n+1}} - 1 \right)} \quad (10)$$

where subscripts “f” and “b” denote the front and back sides of each double-sided multilayer insulation sheet, with N as number of total layers. With small temperature differences between insulation sheets ($T_n \approx T_{n+1}$), the total effective emittance can be provided by the spectral normal emittance integration given in Eq. (8). However, with larger temperature differences between each insulation layer, the total effective emittance must be calculated with

the Planck blackbody temperature–wavelength distribution of each coating face, such that

$$\varepsilon_{f,n} = \int_0^\infty \varepsilon_{f,n}^\lambda \Theta(\lambda, T_n) d\lambda / \sigma T_n^4$$

and

$$\varepsilon_{b,n+1} = \int_0^\infty \varepsilon_{b,n+1}^\lambda \Theta(\lambda, T_{n+1}) d\lambda / \sigma T_{n+1}^4$$

A parameter survey similar to that presented in Supplemental Fig. S3 yielded a backside coating configuration that resulted in a minimum total effective emittance between the front side and the back side of $\varepsilon^* = 3.17 \times 10^{-3}$. The front-side coating is the same as the one presented in Fig. 6b. The backside Ge HCG and Ge-KBr FP parameters are described by $\Lambda = 2.98 \mu\text{m}$, $f = 0.64$, $h = 1.16 \mu\text{m}$ ($h/\Lambda = 0.39$), $d_1 = 0.586 \mu\text{m}$, and $d_2 = 2.087 \mu\text{m}$. This backside configuration alone provides a total normal emittance of $\varepsilon_n = 0.0101$, a TE-polarized emittance of $\varepsilon_{\text{TE}} = 0.0116$, and a TM-polarized emittance of $\varepsilon_{\text{TM}} = 8.70 \times 10^{-3}$. Despite a higher total normal emittance than that of the optimized front side, this back side is designed around spectral minimizations, as seen in Fig. 8b. For instance, where the front side spectral emittance reaches a local maximum at $\lambda = 18.5 \mu\text{m}$, the same wavelength yields a broad local minimum for the back side, where $\varepsilon_{n,\lambda} = 0.0032$. The same can be said for the inverse, where the front side is low, whereas the back side is high emittance at $\lambda = 13 \mu\text{m}$. This complementary design of the back side helps optimize toward the minimum total effective emittance through canceling of the front side's high emittance interference fringes.

Compared to two pristine smooth aluminum faces ($\varepsilon^* = 5.32 \times 10^{-3}$), the front- and back-side optimized FP–HCG coatings can achieve a 1.67 factor e-star reduction per insulation sheet. If calculation of the effective emittance can distinguish linearly polarized TE and TM waves, the polarization-dependent e-stars are $\varepsilon_{\text{TM}}^* = 2.78 \times 10^{-3}$ and $\varepsilon_{\text{TE}}^* = 2.80 \times 10^{-3}$. Realistically, thermal radiative emission and exchange occur without polarization preference. We note that with greater temperature differences between insulation layers, the FP–HCG design for each side can be scaled to minimize spectral normal emittance with Planck blackbody function weighting. Furthermore, this optimization of parameters can be conducted on cryogenic temperature blackbody emission up to temperatures where either the polymer substrate or metal thin film melts: 250°C (operation limit of 150°C) for Mylar and 650°C (operation limit of 250°C) for aluminum.

To illustrate the overall thermal insulation effect of the FP–HCG coating on effective emittance ε^* , Fig. 9 plots several configurations with respect to the number of insulation layers N . The various configurations correspond to single-sided Mylar substrate with oxidized Al (Ox-My), with pristine Al (Al-My), with a single pair Ge–KBr Fabry–Pérot (FP-My) in Fig. 3a, with the optimized FP–HCG (1-D-My) in Fig. 6b, and with the optimized 2-D HCG (2-D-My) in Fig. 7b. With double-sided options, oxidized Al faces the optimized FP–HCG (1-D-Ox), pristine Al faces the optimized FP–HCG (1-D-Al), and front- and back-sided FP–HCG (1-D-F and 1-D-B, respectively) are presented in Fig. 8b. For reference, the total emittances of Mylar, oxidized Al, and pristine Al are given in Fig. 9. The first configuration (Ox-My) is described as the theoretical minimum curve in Ref. [1]. Although FP coated aluminized Mylar outperforms this curve by an effective emittance reduction factor of 1.88, it does not outperform pristine aluminized Mylar (beginning of life). This factor is improved to 2.87 with the 1-D HCG on FP coating; whereas per the discussion on best-case 2-D HCG, this factor is slightly lower at 2.41. The bigger improvement is with double-sided insulation. The improvement factor is 3.80 for the FP-1-D HCG coating with a standard oxidized Al back side; this factor is 1.97 as compared to double-sided oxidized Al. The emittance curve is minimized with the double-coated sheets, which are prescribed by the mismatched

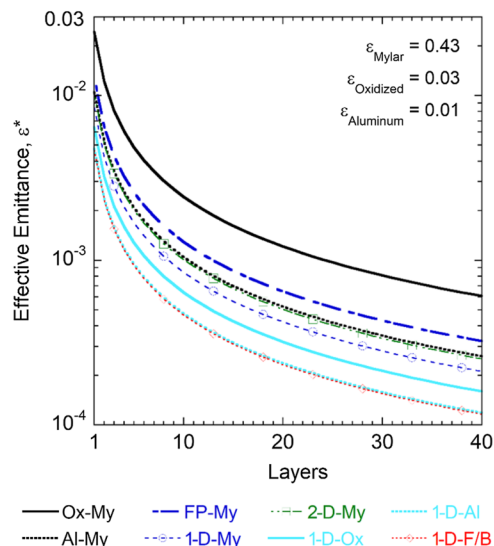


Fig. 9 Theoretical effective emittance curves of various aluminized Mylar blanket configurations, with and without FP–HCG treatments on single or double sides.

FP–HCG in Fig. 8b. This gives a factor of 5.22 over single-sided oxidized aluminized Mylar, and 2.71 over double-sided oxidized aluminized Mylar. The effective emittance reduction factor of a pristine Al back side is about the same, but its performance is likely short-lived. With 40 layers, which in total compose a thick insulation blanket with idealized zero conductance separation construction materials, the effective emittance can reach $\varepsilon^* = 1.16 \times 10^{-4}$. Overall, these effective emittance reduction factors represent the heat flux reduction scaling of multilayer insulations constructed with these augmented coatings.

In the final discussion of this FP–HCG coating, we consider the suitability of the coating materials across different environments with thermal, mechanical, and fluid conditions. Germanium and potassium bromide have high melting temperatures of 938 and 734°C, respectively, beyond the limit for both the polymer substrate and metal thin film. The linear coefficient of thermal expansion of Ge is approximately $6 \mu\text{m}/(\text{m} \cdot ^\circ\text{C})$, whereas KBr has a coefficient of thermal expansion (CTE) of near $40 \mu\text{m}/(\text{m} \cdot ^\circ\text{C})$. With temperature increase, the lack of expansion in the Ge layer means the HCG retains its shape, whereas the high CTE of the underlying layers including the Al and Mylar (30 and $170 \mu\text{m}/(\text{m} \cdot ^\circ\text{C})$, respectively) allows the sheet to bow upward at the edges. Heating of double-sided sheets may put the Ge top layers in tension. Ge, however, has a high tensile modulus of 130 GPa that, given an $\sim 1 \mu\text{m}$ thickness of Ge per side, can exert as much compressive force as a 65- μm -thick (2.5-mil-thick) Mylar substrate in thermal expansion. Although Ge is resistant to water solubility (5 g/L), infrared-transparent salt KBr is water soluble (700 g/L). This may present issues with delamination; but, with large-area Ge gratings, similar characteristic micropatterned surfaces have been found to reduce wettability or increase contact angles with water droplets [66,67]. In addressing the manufacture and construction of these coated flexible insulation sheets, large-area physical vapor sputter deposition chambers and subsequent mask-aligned photolithography can produce variable multilayered gratings on pre-made polished metallized polymer sheets [68–70]. A process flow of this scalable manufacturing method is illustrated in Supplemental Fig. S7. Certainly, a realized coating warrants high-quality spectroscopic reflectance testing with careful handling procedures to ensure thermal radiative insulation performance is protected and prolonged [71,72].

V. Conclusions

This comprehensive paper shows that a dual-material layered coating can achieve normal emittance lower than its pristine metal thin-film substrate. Not only does the inert and dielectric coating

protect the metal against further degradation or oxidation, the proven infrared-transparent germanium surface can also provide ESD, impact, and possibly moisture protection of underlying materials. The broadband ultrahigh reflectance from the surface Ge layer is enabled with a high-contrast grating micropattern. The principles of high reflectance show the HCG period is near wavelength corresponding to blackbody emission, on the order of 2.5 to 3 times smaller than the center wavelength. The best-case HCG width-to-period filling ratio or duty cycle is near 0.6, and the best-case HCG height-to-period ratio is near 0.5. A filling ratio too high reduces the reflectance intensity, despite increasing the number of waveguide modes. A short HCG produces single round-trip Fabry–Pérot resonant modes, allowing near-perfect electromagnetic field cancellation above the plane of the HCG array. The high-index dielectric HCG is combined with a Fabry–Pérot multilayer consisting of Ge and an infrared-transparent low-index cavity layer potassium bromide. Interestingly, the FP layers are not quite described by the quarter-wave thickness law, despite little variation to total emittance with respect to a 10% thickness change. Through random surveying of combined HCG and FP parameters, we understand that wave conditions exiting the HCG and interfering in the near-FP cavity are not the same as those incident.

With some adjustment to the FP thicknesses, while keeping the grating period, filling ratio, and height nearly analytic, a total normal emittance can be lowered to 0.0085, which is below that of its pristine aluminum substrate. Another round of parameter optimization found a back-side FP–HCG coating configuration that results in effective normal emittance of 0.0032. The best design for broadband ultrahigh reflectance HCG includes 1-D grooves, whereas 2-D surface grating micropatterning results in slightly lowered performance. The coating parameters are insensitive to dimensional uncertainty. Despite being a good thermal radiative resistor for the terrestrial room-temperature blackbody, the coating materials present high solar absorptance. Overall, this coating can be physically protective and enhance thermal radiative insulation performance, especially when used as double-sided sheets in a multilayer insulation blanket. The factor of thermal radiative transfer reduction is almost magnitude-fold. With further theoretical investigation and micromanufacturing realization of this coating, more advantageous capabilities could be uncovered. Although the motivation of this coating was originally for radiative insulation of components in the vacuum of space, this coating can also be applied to structural insulation, clothing liners, fire protection, and possibly hydrophobic and antidust treatments.

Acknowledgments

Research was partially funded by the University of North Texas Vice President of Research & Innovation Collaborative College of Science and the College of Engineering Research Seed Funding. The authors thank Morgan A. Blankenship for contributions to our two-dimensional rigorous coupled-wave analysis method.

References

- [1] Gilmore, D. G., and Donabedian, M., *Spacecraft Thermal Control Handbook*, Vol. 1, Fundamental Technologies. Aerospace Press, El Segundo, CA, 2002.
- [2] Sheldahl, L., *The Red Book*. 2009, https://www.sheldahl.com/sites/default/files/2020-02/RedBook_0.pdf.
- [3] Zhang, Z. M., *Nano/Microscale Heat Transfer*, 2nd ed., Springer Nature, London, 2020.
- [4] Palik, E. D., *Handbook of Optical Constants of Solids*. Elsevier Science, New York, 1991.
- [5] Bass, M., and Bennett, J., *Optical Properties of Metals*, Univ. of Southern California, Los Angeles Center for Laser Studies, Los Angeles, CA, 1983, <https://apps.dtic.mil/sti/pdfs/ADA134285.pdf>.
- [6] Kauder, L., *Spacecraft Thermal Control Coatings References*, NASA, 2005, <https://ntrs.nasa.gov/api/citations/20070014757/downloads/20070014757.pdf>.
- [7] Rakić, A. D., “Algorithm for the Determination of Intrinsic Optical Constants of Metal Films: Application to Aluminum,” *Applied Optics*, Vol. 34, No. 22, 1995, pp. 4755–4767. <https://doi.org/10.1364/AO.34.004755>
- [8] Bennett, H., Silver, M., and Ashley, E., “Infrared Reflectance of Aluminum Evaporated in Ultra-High Vacuum,” *Journal of the Optical Society of America*, Vol. 53, No. 9, 1963, pp. 1089–1095. <https://doi.org/10.1364/Journal of the Optical Society of America.53.001089>
- [9] Zhong, Z., and Wang, J., “Uniformity and Characterisation of PVD Aluminium Films,” *Surface Engineering*, Vol. 21, No. 2, 2005, pp. 119–124. <https://doi.org/10.1179/174329405X40939>.
- [10] Henninger, J. H., *Solar Absorptance and Thermal Emittance of Some Common Spacecraft Thermal-Control Coatings*. Vol. 1121, NASA, Scientific and Technical Documents, 1984, <https://ntrs.nasa.gov/citations/19840015630>.
- [11] Dever, J. A., *Low Earth Orbital Atomic Oxygen and Ultraviolet Radiation Effects on Polymers*, NASA, 1991, <https://ntrs.nasa.gov/citations/19840015630>.
- [12] Banks, B. A., and Demko, R., “Atomic Oxygen Protection of Materials in Low Earth Orbit,” *2002 Symposium and Exhibition for the Society for the Advancement of Material and Process Engineering*, Long Beach, CA, 2002.
- [13] Jen, Y. J., Lee, C. C., Lu, K. H., Jheng, C. Y., and Chen, Y. J., “Fabry-Perot Based Metal-Dielectric Multilayered Filters and Metamaterials,” *Optics Express*, Vol. 23, No. 26, 2015, pp. 33,008–33,017. <https://doi.org/10.1364/OE.23.033008>
- [14] Blankenship, M., Adams, K., and Zhang, R. Z., “Gradient-Index Meta-surface Multilayer for Quasioptical Coupling of Infrared Detectors,” *Optical Engineering*, Vol. 60, No. 10, 2021, Paper 107102. <https://doi.org/10.1117/1.OE.60.10.107102>
- [15] Yang, W., Ferrara, J., Grutter, K., Yeh, A., Chase, C., Yue, Y., Willner, A. E., Wu, M. C., and Chang-Hasnain, C. J., “Low Loss Hollow-Core Waveguide on a Silicon Substrate,” *Nanophotonics*, Vol. 1, No. 1, 2012, pp. 23–29. <https://doi.org/10.1515/nanoph-2012-0003>
- [16] Corzine, S. W., Geels, R. S., Scott, J. W., Yan, R. H., and Coldren, L. A., “Design of Fabry-Perot Surface-Emitting Lasers with a Periodic Gain Structure,” *IEEE Journal of Quantum Electronics*, Vol. 25, No. 6, 1989, pp. 1513–1524. <https://doi.org/10.1109/3.29288>
- [17] Kan, Y. H., Zhao, C. Y., and Zhang, Z. M., “Compact Mid-Infrared Broadband Absorber Based on hBN/Metal Metasurface,” *International Journal of Thermal Sciences*, Vol. 130, Aug. 2018, pp. 192–199. <https://doi.org/10.1016/j.ijthermalsci.2018.04.017>
- [18] Fang, X., and Zhao, C. Y., “Unified Analyses and Optimization for Achieving Perfect Absorption of Layered Absorbers with Ultrathin Films,” *International Journal of Heat and Mass Transfer*, Vol. 111, Aug. 2017, pp. 1098–1106. <https://doi.org/10.1016/j.ijheatmasstransfer.2017.04.085>
- [19] Vaughan, J. M., *The Fabry–Perot Interferometer: History, Theory, Practice and Applications*. Routledge, Boca Raton, FL, 2017.
- [20] Wang, L., Basu, S., and Zhang, Z. M., “Direct Measurement of Thermal Emission from a Fabry–Perot Cavity Resonator,” *Journal of Heat Transfer*, Vol. 134, No. 7, 2012, pp. 1–9.
- [21] Taylor, S., Yang, Y., and Wang, L., “Vanadium Dioxide Based Fabry-Perot Emitter for Dynamic Radiative Cooling Applications,” *Journal of Quantitative Spectroscopy and Radiative Transfer*, Vol. 197, Aug. 2017, pp. 76–83. <https://doi.org/10.1016/j.jqsrt.2017.01.014>
- [22] Chao, J., Taylor, S., and Wang, L., “Design and Energy Analysis of Tunable Nanophotonic Infrared Filter Based on Thermochromic Vanadium Dioxide,” *International Journal of Heat and Mass Transfer*, Vol. 186, May 2022, Paper 122515. <https://doi.org/10.1016/j.ijheatmasstransfer.2021.122515>
- [23] Araki, K., and Zhang, R. Z., “An Optimized Self-Adaptive Thermal Radiation Turn-Down Coating with Vanadium Dioxide Nanowire Array,” *International Journal of Heat and Mass Transfer*, Vol. 191, Aug. 2022, Paper 122835. <https://doi.org/10.1016/j.ijheatmasstransfer.2022.122835>
- [24] Huang, M. C., Zhou, Y., and Chang-Hasnain, C. J., “A Surface-Emitting Laser Incorporating a High-Index-Contrast Subwavelength Grating,” *Nature Photonics*, Vol. 1, No. 2, 2007, pp. 119–122. <https://doi.org/10.1038/nphoton.2006.80>
- [25] Chang-Hasnain, C. J., and Yang, W., “High-Contrast Gratings for Integrated Optoelectronics,” *Advances in Optics and Photonics*, Vol. 4, No. 3, 2012, pp. 379–440. <https://doi.org/10.1364/AOP.4.000379>
- [26] Chang-Hasnain, C. J., Ye, Z., Huang, M., and Chase, C., “High-Contrast Grating VCSELs,” *IEEE Journal of Selected Topics in Quantum Electronics*, Vol. 15, No. 3, 2009, pp. 869–878. <https://doi.org/10.1109/JSTQE.2009.2015195>

- [27] Qiao, P., Zhu, L., Chew, W. C., and Chang-Hasnain, C. J., "Theory and Design of Two-Dimensional High-Contrast-Grating Phased Arrays," *Optics Express*, Vol. 23, No. 19, 2015, pp. 24508–24524. <https://doi.org/10.1364/OE.23.024508>
- [28] Karagodsky, V., and Chang-Hasnain, C. J., "Physics of Near-Wavelength High Contrast Gratings," *Optics Express*, Vol. 20, No. 10, 2012, pp. 10,888–10,895. <https://doi.org/10.1364/OE.20.010888>
- [29] Chevallier, C., Fressengeas, N., Jacquet, J., Almuneau, G., Laaroussi, Y., Gauthier-Lafaye, O., Cerutti, L., and Genty, F., "Parameter-Tolerant Design of High Contrast Gratings," *High Contrast Metastructures IV. 2015: International Society for Optics and Photonics, SPIE OPTO*, San Francisco, CA, 2015.
- [30] Zhou, Y., Huang, M. C., Chase, C., Karagodsky, V., Moewe, M., Pesala, B., Sedgwick, F. G., and Chang-Hasnain, C. J., "High-Index-Contrast Grating (HCG) and its Applications in Optoelectronic Devices," *IEEE Journal of Selected Topics in Quantum Electronics*, Vol. 15, No. 5, 2009, pp. 1485–1499. <https://doi.org/10.1109/JSTQE.2009.2021145>
- [31] Qiao, P., Yang, W., and Chang-Hasnain, C. J., "Recent Advances in High-Contrast Metastructures, Metasurfaces, and Photonic Crystals," *Advances in Optics and Photonics*, Vol. 10, No. 1, 2018, pp. 180–245. <https://doi.org/10.1364/AOP.10.000180>
- [32] Zeng, S., Hunt, A., and Greif, R., "Geometric Structure and Thermal Conductivity of Porous Medium Silica Aerogel," *Journal of Heat Transfer*, Vol. 117, No. 4, 1995, pp. 1055–1058. <https://doi.org/10.1115/1.2836281>
- [33] Li, Q., Chen, L., Gadinski, M. R., Zhang, S., Zhang, G., Li, H. U., Iagodkine, E., Haque, A., Chen, L. Q., and Jackson, T. N., "Flexible High-Temperature Dielectric Materials from Polymer Nanocomposites," *Nature*, Vol. 523, No. 7562, 2015, pp. 576–579. <https://doi.org/10.1038/nature14647>
- [34] Jelle, B. P., "Traditional, State-of-the-Art and Future Thermal Building Insulation Materials and Solutions—Properties, Requirements and Possibilities," *Energy and Buildings*, Vol. 43, No. 10, 2011, pp. 2549–2563. <https://doi.org/10.1016/j.enbuild.2011.05.015>
- [35] Cuce, E., Cuce, P. M., Wood, C. J., and Riffat, S. B., "Toward Aerogel Based Thermal Superinsulation in Buildings: A Comprehensive Review," *Renewable and Sustainable Energy Reviews*, Vol. 34, June 2014, pp. 273–299. <https://doi.org/10.1016/j.rser.2014.03.017>
- [36] Ehrenreich, H., Philipp, H., and Segall, B., "Optical Properties of Aluminum," *Physical Review*, Vol. 132, No. 5, 1963, Paper 1918. <https://doi.org/10.1103/PhysRev.132.1918>
- [37] Bright, T. J., Watjen, J. I., Zhang, Z. M., Muratore, C., and Voevodin, A. A., "Optical Properties of HfO₂ Thin Films Deposited by Magnetron Sputtering: From the Visible to the Far-Infrared," *Thin Solid Films*, Vol. 520, No. 22, 2012, pp. 6793–6802. <https://doi.org/10.1016/j.tsf.2012.07.037>
- [38] Bright, T. J., Watjen, J., Zhang, Z. M., Muratore, C., Voevodin, A. A., Koukis, D., Tanner, D. B., and Arenas, D. J., "Infrared Optical Properties of Amorphous and Nanocrystalline Ta₂O₅ Thin Films," *Journal of Applied Physics*, Vol. 114, No. 8, 2013, Paper 083515. <https://doi.org/10.1063/1.4819325>
- [39] Tazawa, M., Kakiuchida, H., Xu, G., Jin, P., and Arwin, H., "Optical Constants of Vacuum Evaporated SiO Film and an Application," *Journal of Electroceramics*, Vol. 16, No. 4, 2006, pp. 511–515. <https://doi.org/10.1007/s10832-006-9908-y>
- [40] Kitamura, R., Pilon, L., and Jonasz, M., "Optical Constants of Silica Glass from Extreme Ultraviolet to Far Infrared at Near Room Temperature," *Applied Optics*, Vol. 46, No. 33, 2007, pp. 8118–8133. <https://doi.org/10.1364/AO.46.008118>
- [41] Kaiser, W., Spitzer, W., Kaiser, R., and Howarth, L., "Infrared Properties of CaF₂, SrF₂, and BaF₂," *Physical Review*, Vol. 127, No. 6, 1962, Paper 1950. <https://doi.org/10.1103/PhysRev.127.1950>
- [42] Bennett, J. M., and Ashley, E., "Infrared Reflectance and Emittance of Silver and Gold Evaporated in Ultrahigh Vacuum," *Applied Optics*, Vol. 4, No. 2, 1965, pp. 221–224. <https://doi.org/10.1364/AO.4.000221>
- [43] Smith, D. R., and Loewenstein, E. V., "Optical Constants of Far Infrared Materials. 3: Plastics," *Applied Optics*, Vol. 14, No. 6, 1975, pp. 1335–1341. <https://doi.org/10.1364/AO.14.001335>
- [44] Zhang, Z. M., Lefever-Button, G., and Powell, F., "Infrared Refractive Index and Extinction Coefficient of Polyimide Films," *International Journal of Thermophysics*, Vol. 19, No. 3, 1998, pp. 905–916. <https://doi.org/10.1023/A:1022655309574>
- [45] Zhang, X., Qiu, J., Li, X., Zhao, J., and Liu, L., "Complex Refractive Indices Measurements of Polymers in Visible and Near-Infrared Bands," *Applied Optics*, Vol. 59, No. 8, 2020, pp. 2337–2344. <https://doi.org/10.1364/AO.383831>
- [46] Tauc, J., Grigorovici, R., and Vancu, A., "Optical Properties and Electronic Structure of Amorphous Germanium," *Physica Status Solidi (b)*, Vol. 15, No. 2, 1966, pp. 627–637. <https://doi.org/10.1002/pssb.19660150224>
- [47] Amotchkina, T., Trubetskov, M., Hahner, D., and Pervak, V., "Characterization of e-Beam Evaporated Ge, YbF₃, ZnS, and LaF₃ Thin Films for Laser-Oriented Coatings," *Applied Optics*, Vol. 59, No. 5, 2020, pp. A40–A47. <https://doi.org/10.1364/AO.59.000A40>
- [48] Green, M. A., and Keevers, M. J., "Optical Properties of Intrinsic Silicon at 300 K," *Progress in Photovoltaics: Research and Applications*, Vol. 3, No. 3, 1995, pp. 189–192. <https://doi.org/10.1002/pip.4670030303>
- [49] Palik, E. D., "Potassium Bromide (KBr)," *Handbook of Optical Constants of Solids*, Elsevier, New York, 1997, pp. 989–1004.
- [50] Querry, M. R., *Optical Constants*, Missouri Univ., Kansas City, 1985, <https://apps.dtic.mil/sti/pdfs/ADA158623.pdf>
- [51] Ordal, M. A., Bell, R. J., Alexander, R. W., Newquist, L. A., and Querry, M. R., "Optical Properties of Al, Fe, Ti, Ta, W, and Mo at Submillimeter Wavelengths," *Applied Optics*, Vol. 27, No. 6, 1988, pp. 1203–1209. <https://doi.org/10.1364/AO.27.001203>
- [52] Ciesielski, A., Skowronski, L., Trzcinski, M., and Szoplik, T., "Controlling the Optical Parameters of Self-Assembled Silver Films with Wetting Layers and Annealing," *Applied Surface Science*, Vol. 421, Nov. 2017, pp. 349–356. <https://doi.org/10.1016/j.apsusc.2017.01.039>
- [53] Tsuda, S., Yamaguchi, S., Kanamori, Y., and Yugami, H., "Spectral and Angular Shaping of Infrared Radiation in a Polymer Resonator with Molecular Vibrational Modes," *Optics Express*, Vol. 26, No. 6, 2018, pp. 6899–6915. <https://doi.org/10.1364/OE.26.006899>
- [54] Moharam, M. G., and Gaylord, T. K., "Rigorous Coupled-Wave Analysis of Metallic Surface-Relief Gratings," *Journal of the Optical Society of America A*, Vol. 3, No. 11, 1986, pp. 1780–1787. <https://doi.org/10.1364/A.3.001780>
- [55] Moharam, M. G., Grann, E. B., Pommet, D. A., and Gaylord, T. K., "Formulation for Stable and Efficient Implementation of the Rigorous Coupled-Wave Analysis of Binary Gratings," *Journal of the Optical Society of America A*, Vol. 12, No. 5, 1995, pp. 1068–1076. <https://doi.org/10.1364/JournaloftheOpticalSocietyofAmericaA.12.001068>
- [56] Araki, K., and Zhang, R. Z., "Mechano-Optical Resonant Emission by Edge Angle Modulation of Wrinkled Graphene on Plasmonic Metal Gratings," *ACS Applied Nano Materials*, Vol. 4, No. 8, 2021, pp. 8399–8407. <https://doi.org/10.1021/acsnm.1c01648>
- [57] Lalanne, P., "Improved Formulation of the Coupled-Wave Method for Two-Dimensional Gratings," *Journal of the Optical Society of America A*, Vol. 14, No. 7, 1997, pp. 1592–1598. <https://doi.org/10.1364/JournaloftheOpticalSocietyofAmericaA.14.001592>
- [58] Chen, Y. B., and Tan, K. H., "The Profile Optimization of Periodic Nano-Structures for Wavelength-Selective Thermophotovoltaic Emitters," *International Journal of Heat and Mass Transfer*, Vol. 53, Nos. 23–24, 2010, pp. 5542–5551. <https://doi.org/10.1016/j.ijheatmasstransfer.2010.06.051>
- [59] Zhao, B., Wang, L., Shuai, Y., and Zhang, Z. M., "Thermophotovoltaic Emitters Based on a Two-Dimensional Grating/Thin-Film Nanostructure," *International Journal of Heat and Mass Transfer*, Vol. 67, Dec. 2013, pp. 637–645. <https://doi.org/10.1016/j.ijheatmasstransfer.2013.08.047>
- [60] Winter, D. F., "Transient Radiative Cooling of a Semi-Infinite Solid with Parallel-Walled Cavities," *International Journal of Heat and Mass Transfer*, Vol. 9, No. 6, 1966, pp. 527–532. [https://doi.org/10.1016/0017-9310\(66\)90088-3](https://doi.org/10.1016/0017-9310(66)90088-3)
- [61] Chang-Hasnain, C. J., and Yang, W., "High-Contrast Gratings for Integrated Optoelectronics," *Advances in Optics and Photonics*, Vol. 4, No. 3, 2012, pp. 379–440. <https://doi.org/10.1364/AOP.4.000379>
- [62] Karagodsky, V., Sedgwick, F. G., and Chang-Hasnain, C. J., "Theoretical Analysis of Subwavelength High Contrast Grating Reflectors," *Optics Express*, Vol. 18, No. 16, 2010, pp. 16973–16988. <https://doi.org/10.1364/OE.18.016973>
- [63] Zhou, Y., Karagodsky, V., Pesala, B., Sedgwick, F. G., and Chang-Hasnain, C. J., "A Novel Ultra-Low Loss Hollow-Core Waveguide

- Using Subwavelength High-Contrast Gratings,” *Optics Express*, Vol. 17, No. 3, 2009, pp. 1508–1517.
<https://doi.org/10.1364/OE.17.001508>
- [64] Araki, K., and Zhang, R. Z., “Simultaneous Solar Rejection and Infrared Emission Switching Using an Integrated Dielectrics-on-VO₂ Metasurface,” *AIP Advances*, Vol. 12, No. 5, 2022, Paper 055205.
- [65] Zhang, R. Z., Liu, X., and Zhang, Z. M., “Modeling the Optical and Radiative Properties of Vertically Aligned Carbon Nanotubes in the Infrared Region,” *Journal of Heat Transfer*, Vol. 137, No. 9, 2015, Paper 091009.
<https://doi.org/10.1115/1.4030222>
- [66] Miljkovic, N., and Wang, E. N., “Condensation Heat Transfer on Superhydrophobic Surfaces,” *MRS Bulletin*, Vol. 38, No. 5, 2013, pp. 397–406.
<https://doi.org/10.1557/mrs.2013.103>
- [67] Kwon, H. M., Paxson, A. T., Varanasi, K. K., and Patankar, N. A., “Rapid Deceleration-Driven Wetting Transition During Pendant Drop Deposition on Superhydrophobic Surfaces,” *Physical Review Letters*, Vol. 106, No. 3, 2011, Paper 036102.
<https://doi.org/10.1103/PhysRevLett.106.036102>
- [68] Marechal, N., Quesnel, E., Juliet, P., and Pauleau, Y., “Radio Frequency Sputter Deposition and Properties of Calcium Fluoride Thin Films,” *Journal of Applied Physics*, Vol. 74, No. 8, 1993, pp. 5203–5211.
- [69] Park, S. H., Lee, K. S., and Reddy, A. S., “Low Emissivity Ag/Si/Glass Thin Films Deposited By Sputtering,” *Solid State Sciences*, Vol. 13, No. 11, 2011, pp. 1984–1988.
<https://doi.org/10.1016/j.solidstatesciences.2011.08.029>
- [70] Seitz, O., Geddes, J. B., III, Aryal, M., Perez, J., Wassei, J., McMackin, I., and Kobrin, B., “Antireflective Surface Patterned by Rolling Mask Lithography,” *Advanced Fabrication Technologies for Micro/Nano Optics and Photonics VII*. International Society for Optics and Photonics, Bellingham, WA, 2014, Paper 89740 V.
- [71] Honner, M., and Honnerová, P., “Survey of Emissivity Measurement by Radiometric Methods,” *Applied Optics*, Vol. 54, No. 4, 2015, pp. 669–683.
<https://doi.org/10.1364/AO.54.000669>
- [72] Miyakita, T., Hatakenaka, R., Sugita, H., Saitoh, M., and Hirai, T., “Development of a New Multi-Layer Insulation Blanket with Non-Interlayer-Contact Spacer for Space Cryogenic Mission,” *Cryogenics*, Vol. 64, Nov.–Dec. 2014, pp. 112–120.
<https://doi.org/10.1016/j.cryogenics.2014.04.008>